Electrical conductivity and ferroelastic properties of Ti-substituted solid solutions (1-x) $BiFeO_3$ – x $Bi_{0.5}K_{0.5}TiO_3$

Espen Tjønneland Wefring[1], Florian H. Schader[2], Kyle G. Webber[2], Mari-Ann Einarsrud[1] and Tor Grande[1]*

[1]Department of Materials Science and Engineering, Norwegian University of Science and Technology, NO-7491, Trondheim, Norway

[2]Institute of Materials Science, Technische Universität Darmstadt, 64287, Darmstadt, Germany

Abstract

The high crystallographic strain and polarization of $BiFeO_3$ are attractive, but utilization of bulk $BiFeO_3$ has been hindered by large leakage current and high coercive field. Here, we report on the electrical conductivity and ferroelasticity of $BiFeO_3$ substituted with 10 and 20 mol% $Bi_{0.5}K_{0.5}TiO_3$. The electrical conductivity is reduced by several orders of magnitude with donor substitution of Fe with Ti, which also suppressed the strong dependence of the conductivity on partial pressure of oxygen. Hard ferroelastic properties of the as-sintered materials were demonstrated by stress-strain measurements. The coercive stress was strongly reduced by quenching from above the ferroelectric to paraelectric phase transition, and the remanent strain increased and coercive stress decreased with increasing temperature up to 400 °C. Ferroelastic hardening was also observed with increasing Ti-donor substitution. The effect of donor substitution is discussed with respect to point defect chemistry and possible hardening mechanisms related to point defects.

KEYWORDS: $BiFeO_3$, donor substitution, conductivity, ferroelasticity

* Corresponding author: grande@ntnu.no

1. Introduction

The search for alternative lead-free piezoelectric materials to replace $Pb(Zr_{1-x}Ti_x)O_3$ (PZT) has gained significant interest in recent years[1], and $BiFeO_3$ (BFO) and BFO-based solid solutions are among the most interesting materials in this respect.[2, 3] BFO is a room temperature rhombohedral multiferroic with a high ferroelectric Curie temperature (T_C, 825 °C), and a large lattice distortion and polarization that prevails up to ~800 °C.[3-6] The high Curie temperature provides potentially large strain and polarization response to an electric field also at elevated temperatures, but utilization of BFO as a piezoelectric material has so far been hindered by large leakage currents and high coercive electric fields (E_C).[2, 7]

The solid solution of (1-x)BFO – $xBi_{0.5}K_{0.5}TiO_3$ (BKT) has been studied by several research groups.[8-15] BKT a is tetragonal ferroelectric at room temperature (T_C = 380 °C)[16], but the rhombohedral polar crystal structure of BFO is stable up to 40 mol% $Bi_{0.5}K_{0.5}TiO_3$ (BKT).[9] It was recently reported that the electrical conductivity of BFO substituted with 10 or 20 mol% BKT was shifted from p-type to n-type conductivity, going through a conductivity minimum, when changing from ambient to inert atmosphere.[15] Moreover, the conductivity of BFO with 30 mol% BKT has been reduced by several orders of magnitude by annealing in inert/reducing atmospheres at selected temperatures.[8, 17] Substitution of Fe^{3+} with, e.g., Ti^{4+} and Nb^{5+} has been shown to reduce the conductivity of BFO, whereas acceptor substitution with, e.g., Ni^{2+} has been shown to increase the conductivity in materials synthesized in air.[18-21] The opposite effect has been demonstrated for acceptor and donor substituted BFO thin films annealed in N_2.[22] There is at present no consistent understanding of the mechanism for the observed reduction of the conductivity with donor substitution, although the concentration of oxygen vacancies and change in the valence of Fe has often been suggested as a plausible mechansism.[2] Finally, it's worth mentioning that the electrical properties of the BFO-materials resembles what has been observed for related oxide perovskites with Fe on the B-site.[23, 24]

BFO can be characterized as a hard ferroelectric, identified by a pinched polarization–electric field hysteresis loop (P-E loop)[7, 25-27] which is the typical behavior of, for example, acceptor doped (substituted) PZT and aged $BaTiO_3$ (BT).[28-30] Hardening is often discussed in relation to point defects where the bulk effect, the domain wall effect and the grain boundary effect are the three main mechanisms normally considered in literature, distinguished mainly by the location of point defects.[29, 31] Hardening is intimately related to aging of the material and arises due to the spontaneous polarization below T_C and sufficient point defect mobility. Soft PZT is achieved by donor

doping or by quenching form above T_C. [29, 32] Softening of BFO has also been demonstrated by qenching[7]. Donor substitution typically reduces the point defect concentration responsible for hardening, while quenching reduces the possibility for migration of the point defects.

The ferroelectric performance of bulk BFO[2, 7, 25, 27] and Ti-substituted BFO[20, 33, 34] has been reported. it has been shown that quenching BFO from above T_C results in softening[7] (de-pinched P-E loop). In the case of the substituted BFO the observations of the P-E loop are often limited to an effect of reduced conductivity as the applied electric field is below E_C.[2, 19, 20, 33, 34] Investigation of the ferroelectric properties of bulk BFO is challenging as high electric fields are required to surpass the coercive electric field, often leading to dielectric breakdown. Mechanical stress-strain measurements may prove useful in this respect as only mechanical load and no electric field is required. Rhombohedral ferroelectrics have domain walls of 71°, 109° and 180° while the ferroelastic switching only occurs for the 71° and 109° domains.[35] The ferroelastic properties of bulk BFO or BFO-based materials have not so far been published, to the best of the authors' knowledge.

Here, we report on the electrical conductivity of $BiFeO_3$ substituted with 10 and 20 mol% $Bi_{0.5}K_{0.5}TiO_3$ as a function of Ti-substitution for Fe, temperature and atmosphere. A significant reduction of the electrical conductivity is reported by Ti-donor substitution and the effect is discussed in relation to the point defect chemistry of the material. The ferroelastic properties of $BiFeO_3$-based materials from ambient temperature up to 400 °C are also reported for the first time. The mechanical stress-strain measurements revealed that the ferroelastic properties depend on the thermal history of the materials. Ferroelastic hardening was observed with increasing Ti substitution and is discussed in terms of crystal structure evolution determined by X-ray diffraction (XRD) and point defect chemistry. Finally, the ferroelectric-to-paraelectric phase transition temperature is determined by differential thermal analysis (DTA) and confirmed by dielectric spectroscopy.

2. Experimental

Ceramic materials with composition $Bi_{0.9}K_{0.1}Fe_{0.8-y}Ti_{0.2+y}O_3$ (0.8BFTy) and ($Bi_{0.95}K_{0.05}Fe_{0.9-y}Ti_{0.1+y}O_3$) (0.9BFTy) were made by solid state synthesis (y= -0.01, 0, 0.01, 0.03, 0.06). Table 1 summarizes the composition and abbreviation used for all the materials. y>0 represents Ti-donor substitution (Fe substituted by Ti) and y<0 acceptor substitution (Ti substituted with Fe). The solid state synthesis and sintering procedure is described elsewhere.[36] The solid state precursors for all the materials were Bi_2O_3 (Aldrich, 99.999 %), K_2CO_3 (Aldrich, 99.99 %), TiO_2 (Aldrich, 99.99 %) and Fe_2O_3 (Aldrich, 99.999 %) except for y = -0.01 and 0.06 where Bi_2O_3 (Aldrich, 99.9 %) and TiO_2 (Aldrich, 99.9 %) were

used. The latter precursors were also used for the samples analyzed by dielectric spectroscopy in various atmospheres (Figure 8). The mixtures of the precursors were calcined (5 h) in an alumina crucible covered with a lid at 820 and 800 °C for 0.8BFTy and 0.9BFTy, respectively. Cylindrical pellets of 0.8BFTy and 0.9BFTy were made by uniaxial and cold isostatic pressing and sintered at 1010 and 980 °C (2 h), respectively, packed in sacrificial powder of the same material.

Phase purity and crystal structure of the materials were investigated by powder X-ray diffraction (XRD) (Siemens D5005 diffractometer with CuKa-radiation and secondary monochromator). The powder was prepared by crushing a sintered pellet with subsequent annealing above T_C to remove possible strain effects due to the milling procedure. Lattice parameters were determined by Pawley fitting using the Topas software.[37] All compositions were refined using the *R*3*c* space group.

The density was measured by Archimedes method and the relative density was calculated using the theoretical density determined from the lattice parameters found by refinement of the XRD data.

The microstructure and grain size of polished (backscattered electrons) and thermally etched (secondary electrons) samples (880 °C, 5 min) was examined using scanning electron microscopy (SEM; Hitachi S-3400N). Energy dispersive X-ray spectroscopy (EDS; X-MAX, Oxford Instruments, UK) was used to confirm the nominal chemical composition.

Differential thermal analysis (DTA; STA 449 C, Netzsch) of all materials was performed on powder prepared the same way as for XRD. The samples were heated (10 °C/min) to 750 (0.8BFTy) and 800 °C (0.9BFTy) in a flow of synthetic air (30 mL/min) and kept at the maximum temperature for 5 min before cooling (10 °C/min).

Dielectric properties were investigated for all compositions with a frequency analyzer (Alpha-A High Performance Frequency Analyser, Novocontrol Technologies) in synthetic air, N_2 and O_2 (Yara Praxair, 5.0). Disc shaped ceramics were used, where 200-300 µm was ground off the parallel surfaces before gold electrodes were sputtered on. One set of samples was heated and cooled (2 °C/min) in synthetic air to/from 400 °C to remove Maxwell-Wagner relaxations[8], before heating cycles to 720 °C (0.8BFTy) and 800 °C (0.9BFTy) were applied. The reported data are from the second high-temperature heating cycle (Figure 5 and 7). A room temperature frequency scan was done before and after every heating cycle, and the reported data are recorded after the second high-temperature heating cycle (Figure 6). A second set of samples was first heated and cooled (2 °C/min, maximum 700 - 800 °C) in synthetic air, then N_2 and finally O_2 (Figure 8). The samples were not removed from the setup between each heating cycle. The activation energy of the conductivity was

determined from an Arrhenius plot of the logarithm of the conductivity versus the inverse temperature in Kelvin.

The cylindrical pellets used for the mechanical stress-strain measurements were ground after sintering to remove surface effects and obtain uniform dimensions (5.8 mm diameter, 6 mm height). Care was taken to ensure that the circular loading faces were parallel. All samples were annealed 30 min above T_C (710 °C for 0.8BFTy and 780 °C for 0.9BFTy) to remove any internal stress fields or domain reorientation caused by the machining process. This was also done between each experiment where load was applied. The samples were subsequently cooled either in the furnace (300 °C/h) or quenched by removing the sample from the furnace at $T>T_C$ for cooling in air. The quenching of the samples did not result in microcracking. The heat treatments were done on an alumina plate covered by an alumina crucible, and in the presence of sacrificial powder of the same composition to reduce evaporation of bismuth and potassium. All quenched samples were tested within 14 hours after quenching.

Stress-strain measurements were performed in a load frame (Z030, Zwick GmbH & Co.KG) able to apply uniaxial compressive stress and with a spilt furnace (SV800, Thermal Technology GmbH) for heating. A detailed description of the experimental setup can be found elsewhere.[38] A preload (100 N) was applied before each measurement to ensure alignment and contact. Loading and unloading was done with a constant rate (4 MPa/s) and the maximum load was selected according to the desired output of the measurement. The loading cycle was in some cases aborted before the pre-programmed maximum load was reached to prevent breakage of sample or equipment. Measurements at elevated temperature were done at 100, 200, 300 and 400 °C. A heating rate of 300 °C/h was used with a dwell time of 5-15 min at the set temperature (shorter time at higher temperature) to allow temperature stabilization before load was applied. The aging process of 0.8BFT0 was specifically studied by adding a dwell time of 2 and 7 h at 400 °C before applying load to a quenched sample. A typical ferroelastic hysteresis curve can be partially characterized by the coercive stress (σ_C), defined as the inflection point in the stress-strain response during loading, and the remanent strain (ε_r), which is the remaining plastic strain after unloading.[39] The strain was corrected for instrumental contributions. The coercive stress was determined as the minimum of the first derivative of stress with respect to strain ($d\sigma/d\varepsilon$). The error for measured remanent strain is estimated to 2 % and the overall error for the ferroelastic measurement is estimated to 5 %.[38, 40]

3. Results

Polycrystalline ceramics in the two composition series 0.8BFTy and 0.9BFTy were successfully prepared by the solid state synthesis procedure. The ceramics were dense (≥96 % of theoretical density) and micrographs of the microstructure are shown in Figure 1. The grain size, summarized in Table 1, was submicron for all materials except 0.8BFT-1 and 0.8BFT6 where significant grain growth was evident particularly for 0.8BFT-1. In case of 0.8BFT6 the grain growth can possibly be related to the presence of a secondary phase as described further below. The nominal composition of the materials was confirmed by EDS.

All the materials were phase pure according to room temperature XRD except 0.8BFT6, 0.8BFT3 and 0.9BFT6 (Figure 2a). The secondary phase observed for 0.8BFT3 and 0.9BFT6 (Figure 2a) was not observed by XRD on the bulk as-sintered ceramics, but appeared in the diffractograms of crushed and annealed powders. SEM investigation of polished pellets (not thermally etched) using backscatter electrons displayed phase pure composition except for 0.8BFT6 where an Aurivillius phase (Ti and Bi rich) was identified by EDS. Based on the SEM and XRD data the solubility limit for Ti was reached for the highest Ti-donor substitutions (0.8BFT3, 0.8BF6 and 0.9BFT6).

The rhombohedral splitting of the diffraction lines decreased significantly with increasing Ti-substitution (y>0) as shown in Figure 2b (0.8BFTy) and Figure 2c (0.9BFTy). This is further reflected by the change in the lattice parameters with increasing Ti-substitution displayed in Figure 3a and the rhombohedral lattice distortion, which is significantly reduced (Figure 3b). The effect of Ti-substitution is more pronounced for 0.8BFTy than for 0.9BFTy.

Table 1) Composition and corresponding abbreviation of all synthesized materials along with room temperature lattice parameters and grain size of sintered ceramics.

Composition	Abbreviation	Lattice parameter a, [Å]	Lattice parameter c, [Å]	Lattice distortion, c_{pc}/a_{pc}	Grain size, [µm]
$Bi_{0.90}K_{0.10}Fe_{0.81}Ti_{0.19}O_3$	0.8BFT-1	5.580(7)	13.844(3)	1.013	5.5 ± 0.2
$Bi_{0.90}K_{0.10}Fe_{0.80}Ti_{0.20}O_3$	0.8BFT0	5.589(2)	13.809(8)	1.009	0.9 ± 0.09
$Bi_{0.90}K_{0.10}Fe_{0.79}Ti_{0.21}O_3$	0.8BFT1	5.597(2)	13.74(0)	1.002	0.7 ± 0.1
$Bi_{0.90}K_{0.10}Fe_{0.77}Ti_{0.23}O_3$	0.8BFT3	5.602(1)	13.73(2)	1.001	0.9 ± 0.08
$Bi_{0.90}K_{0.10}Fe_{0.74}Ti_{0.26}O_3$	0.8BFT6	5.600(6)	13.72(7)	1.001	1.2 ± 0.09
$Bi_{0.95}K_{0.05}Fe_{0.90}Ti_{0.10}O_3$	0.9BFT0	5.582(7)	13.847(0)	1.013	0.6 ± 0.03
$Bi_{0.95}K_{0.05}Fe_{0.89}Ti_{0.11}O_3$	0.9BFT1	5.584(7)	13.837(3)	1.012	0.6 ± 0.05
$Bi_{0.95}K_{0.05}Fe_{0.87}Ti_{0.13}O_3$	0.9BFT3	5.586(3)	13.79(7)	1.008	0.6 ± 0.02
$Bi_{0.95}K_{0.05}Fe_{0.84}Ti_{0.16}O_3$	0.9BFT6	5.594(1)	13.76(9)	1.005	0.7 ± 0.04

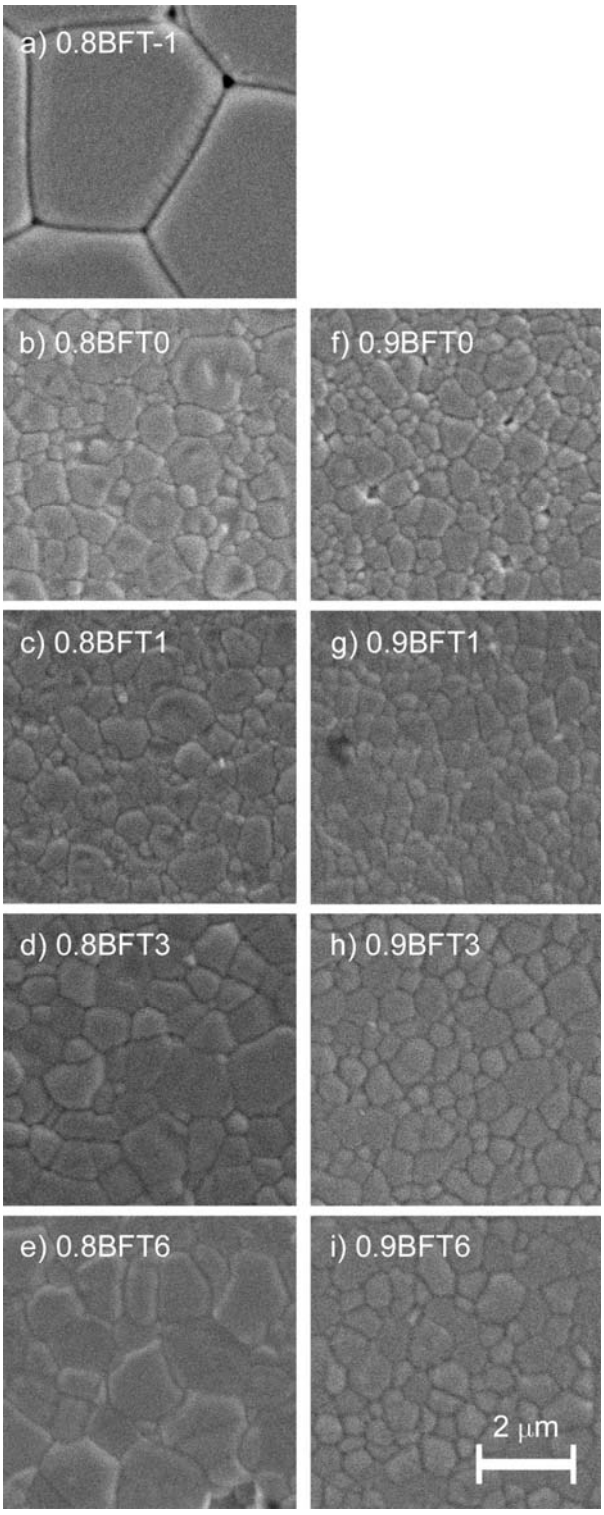

Figure 1) SEM micrographs (secondary electrons) of polished and subsequently thermally etched 0.8BFTy and 0.9BFTy.

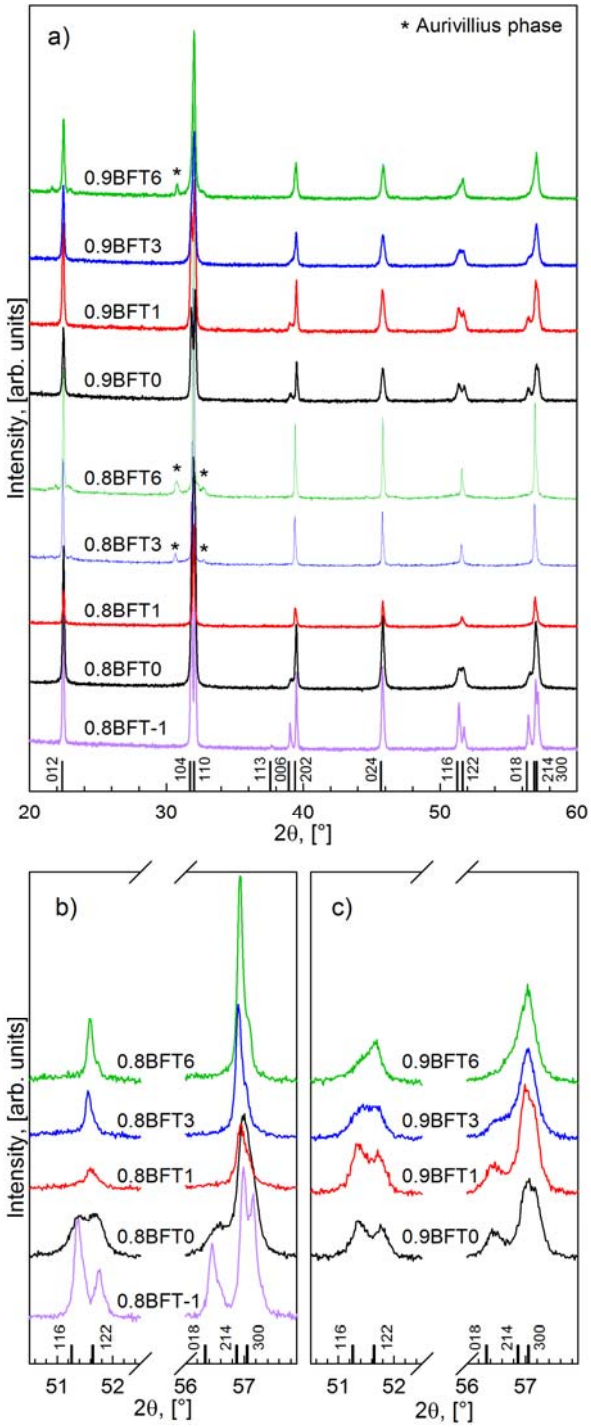

Figure 2) a) Room temperature XRD of 0.8BFTy and 0.9BFTy; b) and c) Selected diffraction lines of 0.8BFTy and 0.9BFTy, respectively, emphasizing decreasing rhombohedral splitting with increasing y.

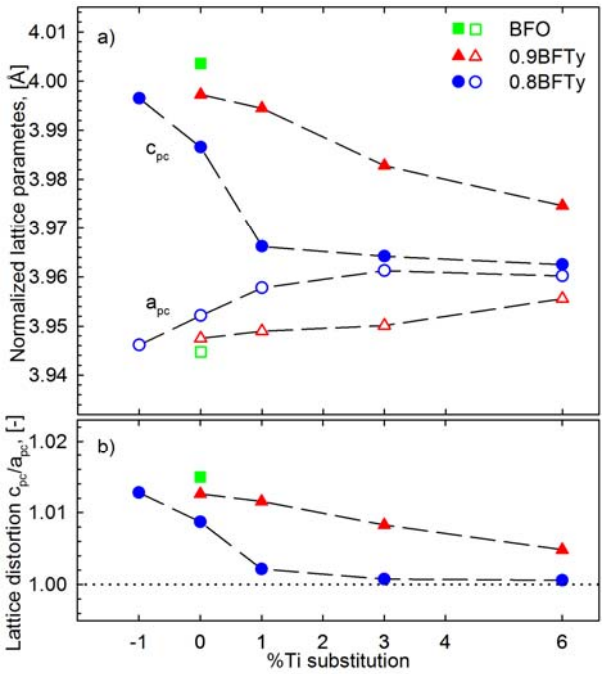

Figure 3) Refined normalized lattice parameters of 0.8BFTy and 0.9BFTy as a function of Ti-substitution at room temperature (a) and the corresponding lattice distortion c_{PC}/a_{PC} (b). Data for 1.0BFT0 are taken from elsewhere.[5] The lattice parameters were normalized according to the following; $a_{pc} = 2^{-½}a_h$ and $c_{pc} = 12^{-⅓}c_h$ where pc and h denote pseudo cubic and hexagonal, respectively. Dashed and dotted lines serve as guide to the eye.

The ferroelectric-to-paraelectric phase transition was demonstrated by an endothermic (exothermic) event during heating (cooling) using DTA as shown in Figure 4. The onset temperature of the peak and the temperature at the maximum (minimum) during heating (cooling) are summarized in Table 2. A hysteresis between heating and cooling confirms the 1st order nature of transition for all the materials. Two peaks are evident for the two non-substituted materials (0.9BFT0 and 0.8BFT0) pointing to two successive phase transitions as reported for pure BFO.[41] The phase transition is significantly sharper for the acceptor substituted material (0.8BFT-1) and donor substituted 0.9BFTy materials. The phase transition is shifted to slightly higher temperatures with donor substitution for both composition series.

The ferroelectric-to-paraelectric phase transition observed by DTA was further confirmed by dielectric spectroscopy based on the permittivity recorded during heating (Figure 5). The loss tangent (not shown) increased strongly towards the phase transition. The temperature at the permittivity maximum, summarized in Table 2, does not show a strong dependence on the Ti-substitution level except for the acceptor substituted material (0.8BFT-1) which has a lower

transition temperature. The permittivity of the 0.9BFTy (y<0.06) materials could not be determined around T_C due to high conductivity. Relaxation in the permittivity, seen for 0.8BFT0 and 0.8BFT1 around 580 °C and for 0.9BFT6 near 680 °C, a, is proposed to be related with movement of point defects as further discussed below.

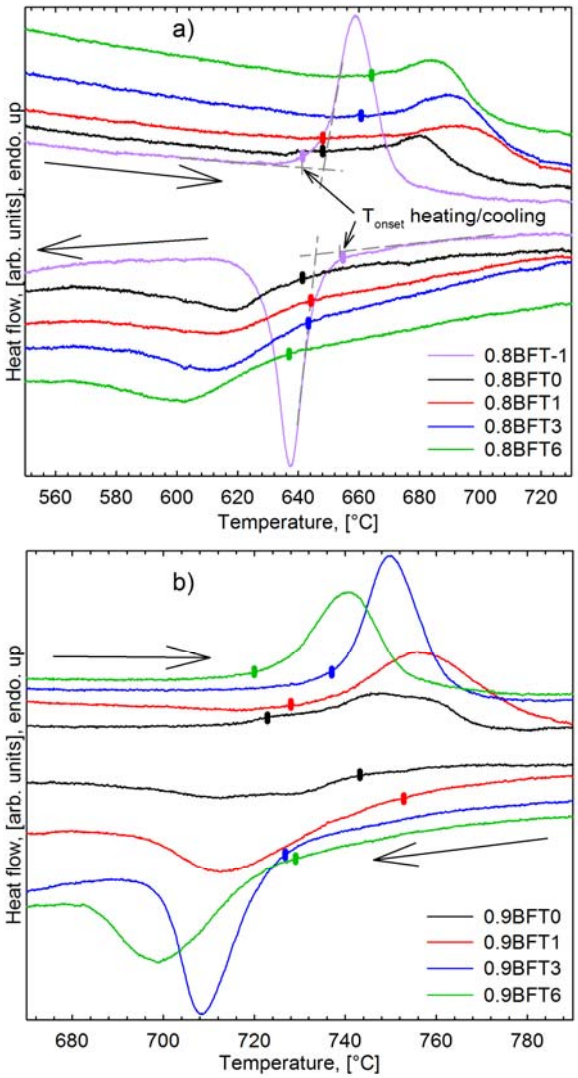

Figure 4) DTA heat flow signal for 0.8BFTy and 0.9BFTy materials during heating and cooling. The grey lines indicate the method for determining the onset temperature of a peak. The onset temperature for each composition is indicated by a colored dot and was determined by the midpoint between the crossing dashed lines and the separation of the data curve and the “horizontal” dashed line.

Table 2) Phase transition temperatures of 0.8BFTy and 0.9BFTy determined by DTA and measurements of the dielectric permittivity.

Material	DTA				Permittivity	
	Onset, heating	Maximum, heating	Onset, cooling	Minimum, cooling	Maximum, heating	Maximum, cooling
	[°C]	[°C]	[°C]	[°C]	[°C]	[°C]
0.8BFT-1	642 ± 10	659 ± 1	654 ± 10	637 ± 1	656 ± 15	625 ± 15
0.8BFT0	648 ± 15	680 ± 1	641 ± 5	619 ± 1	675 ± 15	620 ± 15
0.8BFT1	648 ± 10	694 ± 1	644 ± 10	613 ± 1	677 ± 15	638 ± 15
0.8BFT3	661 ± 10	688 ± 1	643 ± 10	612 ± 1	675 ± 15	645 ± 15
0.8BFT6	664 ± 10	684 ± 1	637 ± 10	602 ± 1	672 ± 15	639 ± 15
0.9BFT0	723 ± 10	746 ± 1	743 ± 10	727 ± 1	-	-
0.9BFT1	728 ± 10	756 ± 1	753 ± 10	713 ± 1	-	-
0.9BFT3	737 ± 10	750 ± 1	727 ± 10	709 ± 1	-	-
0.9BFT6	720 ± 10	740 ± 1	729 ± 10	699 ± 1	720 ± 15	703 ± 15

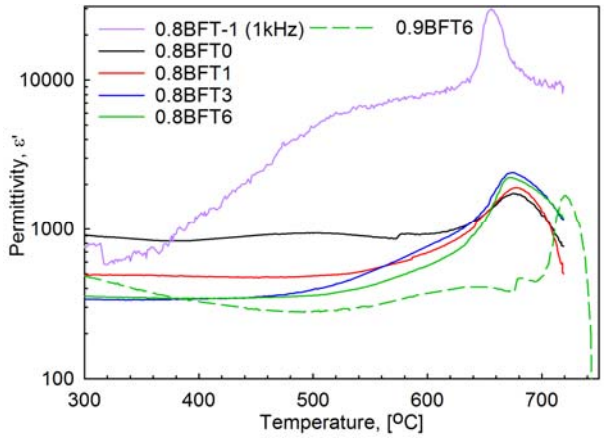

Figure 5) The real permittivity (10kHz) as a function of temperature during heating for 0.8BFTy and 0.9BFT6.

The conductivity of 0.8BFT0 and 0.9BFT0 was significantly reduced by donor substitution both at room temperature (Figure 6) and at elevated temperature (Figure 7). Substitution of 1 mol% Fe^{3+} with Ti^{4+} (y = 0.01) reduced the conductivity of 0.8BFT0 and 0.9BFT0 at 10 mHz by four and two orders of magnitude, respectively (Figure 6). No further significant reduction of the conductivity was observed with y > 0.01. The conductivity of 0.8BFT-1 was higher relative to 0.8BFT0, a case that corresponds to acceptor substitution where Ti^{4+} is substituted by Fe^{3+} (Figure 6a and 7a).

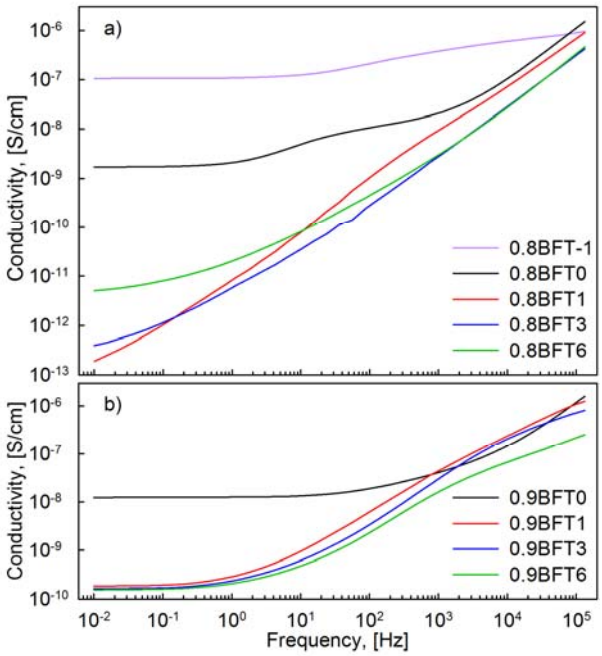

Figure 6) The real part of the AC conductivity at room temperature as a function of frequency for 0.8BFTy (a) and 0.9BFTy (b). Both (a) and (b) have the same y-axis scale for direct comparison.

The effect of Ti^{4+} substitution on the conductivity is evident up to the phase transition temperature for both 0.8BFTy and 0.9BFTy series, shown in Figure 7a and 7b, respectively. The conductivity within each series converges towards a similar value for all the materials in each series when approaching the phase transition and the temperature dependence of the conductivity become comparable. A significant shift in the activation energy is observed around 500 °C, where both the activation energy and the conductivity of all the donor substituted materials converge (Figure 7). 0.8BFT-1 and 0.8BFT0 also show a slightly decreasing conductivity at the ferroelectric-to-paraelectric phase transition, while for all other materials the conductivity demonstrates a weak increase at the phase transition, as highlighted in the insets in Figure 7.

The real AC conductivity of 0.8BFT0, 0.8BFT1 and 0.8BFT3 was measured in different atmospheres at elevated temperature, and the data are shown in Figure 8. Several interesting features were observed. The conductivity is clearly reduced when heating 0.8BFT0 (Figure 8a) in N_2, compared to the conductivity in synthetic air, in the temperature range ~400-500 °C. This reduction is smaller for 0.8BFT1 (Figure 8b) and not visible for 0.8BFT3 (Figure 8c). The conductivity measured in N_2 increases (relative to that in synthetic air) from ~500 °C and has surpassed the conductivity measured in synthetic air at 700 °C for both 0.8BFT1 and 0.8BFT3. Subsequent heating in O_2 (after cooling in N_2) shows an increased conductivity for 0.8BFT0 and a reduced conductivity for 0.8BFT1

and 0.8BFT3 at 700 °C. The difference between conductivity measured in O_2 (heating) and N_2 (cooling) was evident already at ~270 °C, implying a significant mobility of oxygen ions at this low temperature.[15,17]

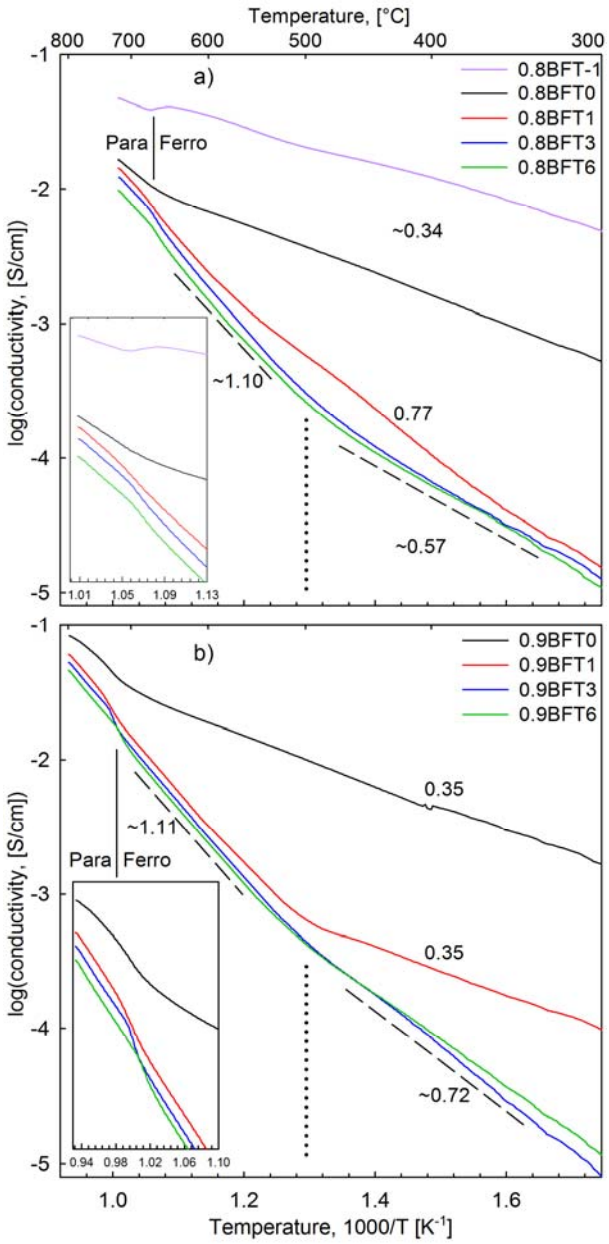

Figure 7) The real part of the AC conductivity (100 Hz) vs. temperature during heating for 0.8BFTy (a) and 0.9BFTy (b) above 300°C where the conductivity was observed to be frequency independent. Activation energies are given as eV. The dotted lines mark a shift for the activation energy near ~500 °C. Insert: Conductivity in the temperature range close to the ferroelectric phase transition.

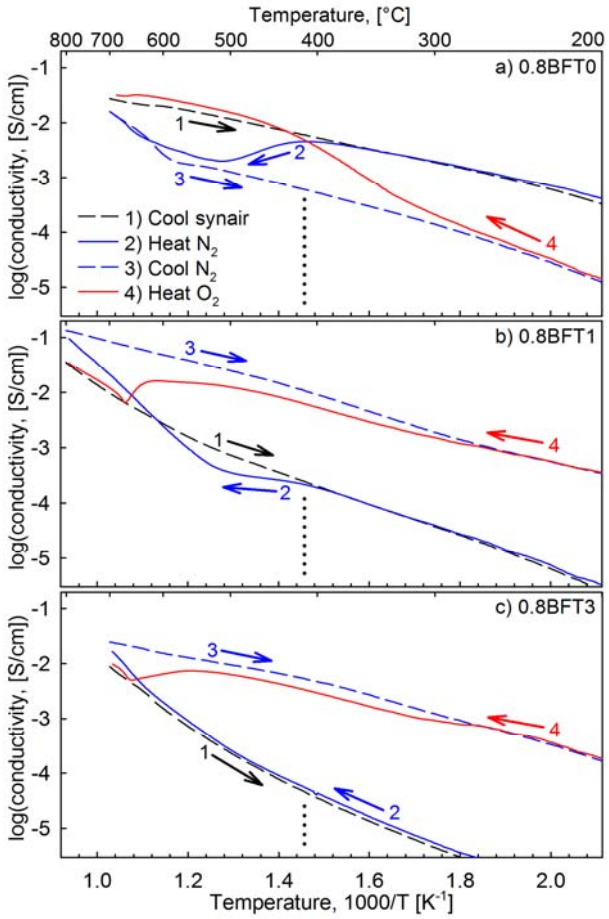

Figure 8) The real part of the AC conductivity (10kHz) vs. temperature in 0.8BFT0, 0.8BFT1 and 0.8BFT3. The numerated arrows denote the order of heat treatment with cooling in synthetic air (1), heating in N_2 (2), cooling in N_2 (3) and heating in O_2 (4).

The mechanical behavior of the materials was investigated by applying a uniaxial compressive stress and recording the strain response. The mechanical stress-strain behavior of 0.8BFT0 and 0.8BFT3 annealed above T_C and cooled with 300 °C/h is shown in Figure 9a. A nearly linear elastic response is observed for both materials, marked by a relatively small remanent strain and minor mechanical hysteresis. A hysteresis loop and development of larger remanent strain is observed for both materials after quenching the samples in air from above T_C (Figure 9b). 0.8BFT0 shows a more pronounced opening of the hysteresis loop than 0.8BFT3 after quenching giving a larger ε_r, which is expected to partially originate from the significantly larger lattice distortion observed for 0.8BFT0 (Table 1).

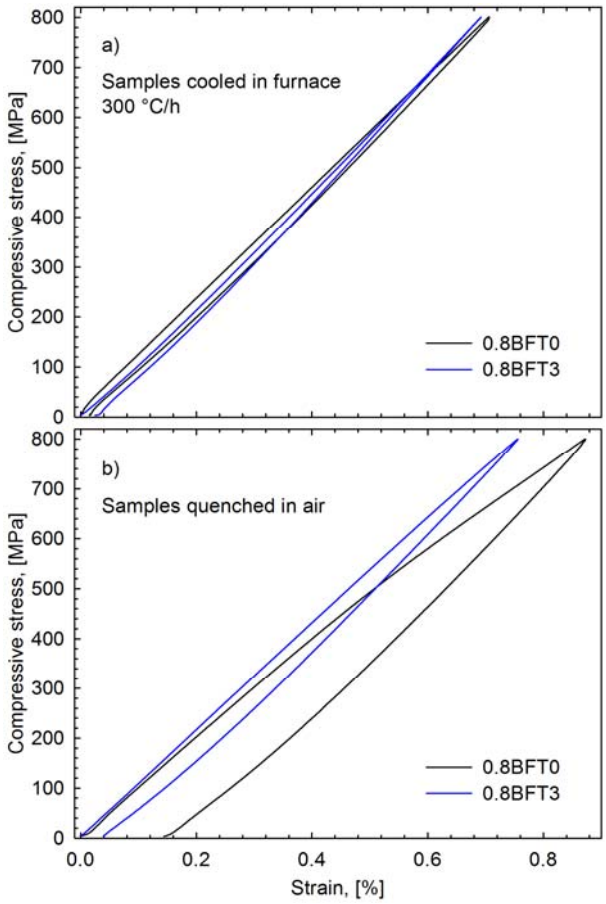

Figure 9) The room temperature stress-strain behavior of 0.8BFT0 and 0.8BFT3 after furnace cooling 300 °C/h (a) and air quenching (b).

The development of the ferroelastic hysteresis loop from room temperature to 400 °C is shown for 0.8BFTy and 0.9BFTy in Figure 10. A thermally activated domain switching behavior is inferred, where ε_r increases with increasing temperature up to 200 °C (Figure 11a, maximum load σ_{max} = 800 MPa). ε_r of both 0.8BFT1 and 0.8BFT3 is small at room temperature, while a significant increase in ε_r was observed at 100 °C and 200 °C, respectively. This reflects the lowered coercive stress as the temperature increases, shown in Figure 11b. σ_C is the stress where the domain switching rate is highest and as $\sigma_{max} > \sigma_C$ for 0.8BFT1 at 100 °C, this is the temperature where a significant increase of ε_r occurs. The same effect is responsible for the increased ε_r observed for 0.8BFT3 at 200 °C.

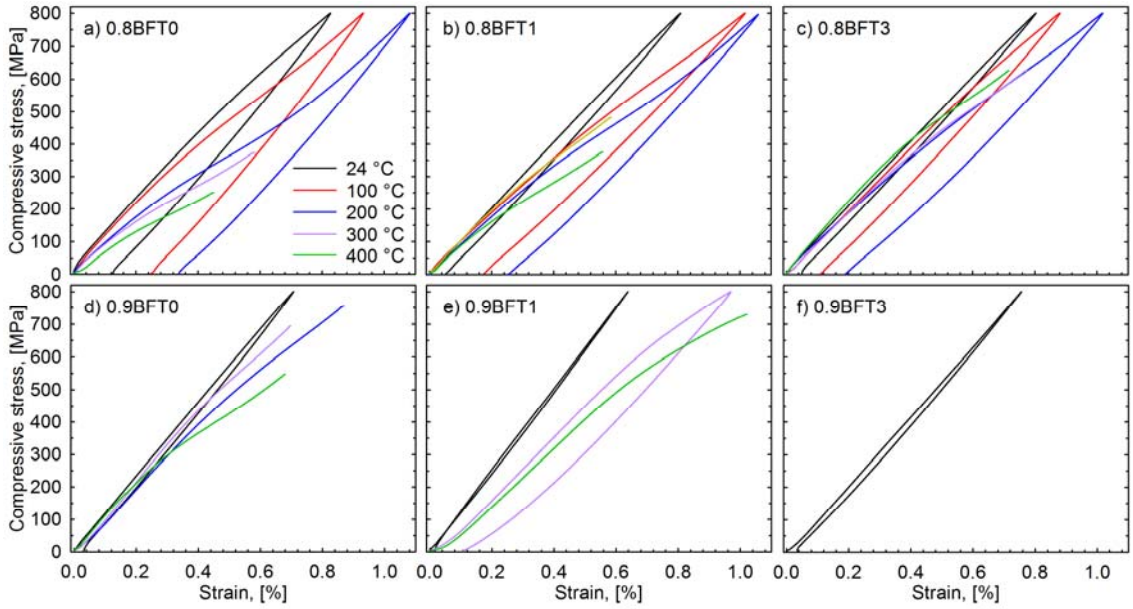

Figure 10) Ferroelastic hysteresis loops of air quenched 0.8BFT0 (a), 0.8BFT1 (b) and 0.8BFT3 (c) from room temperature to 400 °C.

The coercive stress of 0.8BFT0, 0.8BFT1, 0.8BFT3 and 0.9BFT0 decreases significantly with increasing temperature (Figure 11b). A hardening effect (increasing σ_C) on both 0.8BFTy and 0.9BFTy is observed with increasing Ti-substitution (Figure 11b). The stress-strain curve of a normally cooled 0.8BFT0 sample (not shown) and a quenched 0.9BFT1 sample (Figure 10e) was measured at 400 °C up to 665 and 730 MPa, respectively, without surpassing σ_C and it is estimated that σ_C > 800 MPa for both. The coercive stress at 400 °C of air quenched 0.8BFT0 increased by annealing at 400 °C before applying load (inset, Figure 11b).

1. Discussion

4.1 Electrical conductivity

The electrical conductivity of 0.8BFTy and 0.9BFTy was clearly reduced as a result of donor substitution with Ti^{4+} (Figure 6 and 7). This behavior is in line with what is expected for p-type conductors and also in line with what has been observed elsewhere.[19-21, 24, 42] The real AC conductivity of 0.8BFTy is reduced by up to four orders of magnitude in the investigated frequency range (Figure 6), which is amongst the largest reductions reported in literature for BFO materials. Extrapolation of the measured conductivities towards lower frequencies indicates that the reduction with respect to the DC conductivity is even larger. The effect of Ti-substitution is less pronounced in

the high frequency regime, which shows that the reduction mainly stems from a reduced DC conductivity. This is important as utilization of high E_C materials depend on a high applied DC electric field without inducing currents that may lead to dielectric breakdown of the material. The real AC conductivity of 0.9BFTy shows a frequency independent conductivity at the lower frequencies, and the conductivity reduction is smaller than for 0.8BFTy. The effects of Ti substitution will be further discussed below.

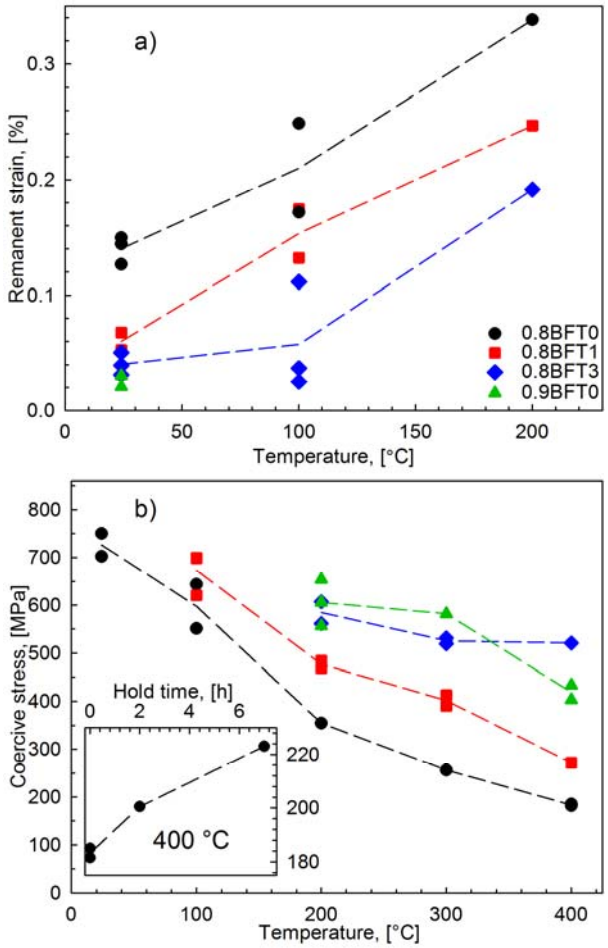

Figure 11) Remanent strain (a) and the coercive stress (b) of 0.8BFTy and 0.9BFT0 as function of temperature. The inset in (b) shows the coercive stress of 0.8BFT0 at 400 °C after holding at 400 °C for 0, 2 and 7 hours. The maximum load applied was 800 MPa up to 200 °C, and $>\sigma_C$ above 200 °C. All samples were air quenched from $>T_C$ prior to the measurement. All measurements are plotted and the dashed lines act as a guide to the eye along the path of average value for each temperature.

It is evident that the electrical conductivity of 0.8BFT0 and 0.9BFT0 depended on the thermal and atmospheric history of the ceramics (Figure 8) as previously reported for related materials.[8, 15, 17, 43] The conductivity goes through a minimum upon decreasing the partial pressure of oxygen, moving from p-type to n-type semiconductor behavior.

Donor-substitution of Ti^{4+} on the Fe^{3+} site in BFO is proposed to be charge compensated by annihilation of oxygen vacancies ($V_O^{\bullet\bullet}$) as shown in Eq. (1).

$$TiO_2 + Fe_{Fe}^{\times} + 1/2\,V_O^{\bullet\bullet} \xrightarrow{BFO} Ti_{Fe}^{\bullet} + 1/2\,Fe_2O_3 + 1/2\,O_O^{\times} \quad (1)$$

The concentration of $V_O^{\bullet\bullet}$ is closely related to the valence of Fe through Eqs. (2) and (3).

$$2Fe_{Fe}^{'} + 1/2\,O_2 + V_O^{\bullet\bullet} \rightleftharpoons 2Fe_{Fe}^{\times} + O_O^{\times} \quad (2)$$

$$2Fe_{Fe}^{\times} + 1/2\,O_2 + V_O^{\bullet\bullet} \rightleftharpoons 2Fe_{Fe}^{\bullet} + O_O^{\times} \quad (3)$$

The reduction of the concentration of oxygen vacancies by Ti donor substitution will shift Eqs. (2) and (3) towards the left, which results in a reduction of the valence of Fe. The non-substituted materials have p-type (Fe^{4+}) conductivity in air[15] and the strong reduction of the electrical conductivity with Ti donor substitution is therefore qualitatively explained by a reduction of the concentration of electron holes (Fe^{4+}). This is analogous to a shift of the conductivity minimum (observed at a given partial pressure of oxygen for 0.8BFT0 and 0.9BFT0[15]) towards higher partial pressures of oxygen. This is further supported by the data shown in Figure 8. A pronounced reduction in the conductivity can be observed between approximately 400 and 500 °C for 0.8BFT0 (Figure 8a). This reduction is less pronounced for 0.8BFT1 (Figure 8b) and not observable for 0.8BFT3 (Figure 8c), which infer that the n-type conductivity is more noticeable with increasing substitution level and that the electron hole (Fe^{3+}) concentration is reduced (making p-type conductivity less pronounced). The conductivity is seen to increase directly (without a preceding reduction) when 0.8BFT3 is heated in N_2, demonstrating that the material is an n-type conductor. We therefore conclude that Ti donor substitution is charge balanced by annihilation of oxygen vacancies and reduction of the electron hole concentration, giving n-type conductivity in line with point defect equilibria (1)-(3).

In the same way that donor substitution reduces the conductivity of 0.8BFTy, acceptor substitution increases the conductivity, as shown for 0.8BFT-1 (Figure 6a and 7a). In this case Fe^{3+} replaces Ti^{4+}, which is charge compensated by formation of $V_O^{\bullet\bullet}$ as illustrated by the defect equilibrium in Eq. (4).

$$1/2\,Fe_2O_3 + Ti_{Ti}^{\times} + 1/2\,O_O^{\times} \xrightarrow{BFO} Fe_{Ti}^{'} + TiO_2 + 1/2\,V_O^{\bullet\bullet} \quad (4)$$

This creates more electron hole charge carriers that increase the conductivity in p-type conductors as Eqs. (2) and (3) are shifted to the right.

The donor substituted materials (y > 0) display an increased activation energy relative to the acceptor and non-substituted materials (y ≤ 0). The activation energy for the y = 0 and y = -0.01 materials is equal to the values reported for 0.7BFT0 by Morozov et al.[8] for $\sigma_{DC,bulk}$ near 400 °C. The activation energies are also comparable to values reported for Ca- and Nb-substituted BFO.[18, 44] The activation energy of the conductivity measured in N_2 increases and that measured in O_2 decreases significantly in donor substituted materials around ∼500 °C (Figure 8). This shift in the activation energy is attributed to the formation/removal of charge carriers described by Eq. (2) and (3). Below this temperature these tow defect equilibria is frozen in due to not sufficient ionic mobility and do not contribute to the change in the charge carrier concentration below 500 °C in these experiments. The shift corresponds well with the increased activation energy observed at 500 °C for donor substituted materials in Figure 7.

4.2 Stress-strain behavior

It is evident from the ferroelastic hysteresis curves reported in Figure 9 that quenching the material from above T_C leaves the material ferroelastically softer and increases the remanent strain. This is analogous to ferroelectric properties of quenched and non-quenched samples of BFO and BT.[7, 28] Based on related observations of the strain-stress hysteresis in PZT[45], we propose that point defects are the main reason for pinning of domain walls also in BFO. Point defects are randomly distributed in the crystal lattice in the paraelectric and paraelastic state above T_C. The random distribution is frozen in by rapid cooling (quenching) due to the lack of sufficient point defect mobility at low temperature, preventing point defect ordering that subsequently pin domain walls. A slow cooling rate will on the other hand allow the formation, and more importantly reorientation, of point defects clusters as both the driving force (spontaneous polarization and possibly also strain) *and* point defect mobility will be present simultaneously. Oxygen and oxygen vacancies are mobile down to at least ∼270 °C (Figure 8). Annealing a quenched sample at 400 °C should hence result in re-hardening of the materials (remove the effect of quenching) and thereby re-establish a higher coercive stress as is observed in the inset of Figure 11b. The hardening of PZT and BT is also suggested to be a result of oxygen vacancy migration where the spontaneous polarization of the unit cell leaves the energy of the oxygen sites in the unit cell non-degenerate.[28, 29] Based on the results

and discussion presented herein it is suggested that oxygen vacancies are an important constituent to the hardening observed in BFO. The data are, however, not sufficient to determine the exact mechanism for the hardening.

Donor substitution with Ti^{4+} for Fe^{3+} in both 0.8BFTy and 0.9BFTy gives an apparent ferroelastic hardening, where an increased coercive stress is observed with increasing donor substitution (Figure 11b). This is opposite of what has previously been reported for PZT, where donor substitution clearly softens the material.[32, 46] The present data suggest that ordering of oxygen vacancies cannot be the sole reason for the hardening observed in BFO as the concentration of $V_O^{\bullet\bullet}$ is expected to be lowered by donor substitution. The hardening effect of donor substitution has not been reported previously. Earlier reports have shown the pinched P-E loop of donor substituted BFO, but the observed effect is probably related to a reduced conductivity rather than hardening/softening as sub-coercive electric fields are often used.[2, 19, 33, 34] The reduced permittivity with increasing Ti substitution is also an indication of a hardened ferroelectric (Figure 5).[30] The origin of the huge relaxation observed for 0.8BFT-1 is unknown (Figure 5). It should be noted that the removal of oxygen vacancies by Ti substitution is accompanied by an altered concentration of charge carriers (related to the valence of Fe) as discussed in the previous paragraph. It has been shown by others that the conductivity of the domains in BFO is different from that of the domain walls and that the conductivity of domain walls can be tuned by annealing in different atmospheres.[2, 47-50] The understanding of point defects in BFO presented here and elsewhere is not sufficient to determine whether the valence of Fe in the domain and at the domain wall have similar dependencies on atmosphere. It has been discussed but not concluded on whether this domain wall behavior is of importance for the domain switching properties of BFO.[2]

The crystal structure of 0.8BFTy and 0.9BFTy (Figure 2 and 3) changed significantly with Ti substitution. The lattice distortion (c_{pc}/a_{pc}) of 0.8BFT0 decreased ~75 % with only 1 mol% Ti substitution, which is much more severe than for 0.9BFTy (Figure 3b). The reduced lattice distortion has also been observed by others for Ti substitution in pure BFO but to a smaller extent.[51] The effect of quenching is mainly related to the distribution of point defects in the lattice and following the discussion earlier in this section it is expected that the oxygen vacancy concentration in 0.8BFT3 is lower than in 0.8BFT0. However, the smaller lattice strain combined with the higher coercive stress is most likely the explanation for the lower remanent strain and the less pronounced effect of quenching for 0.8BFT3 relative to 0.8BFT0.

Previous work on La substituted BFO-$PbTiO_3$ has shown that a reducing lattice distortion was accompanied by a decreasing σ_C down to c/a = 1.01.[39] In this work we observe that σ_C increases with

decreasing c/a (Figure 3 and 11). It is noted that the c/a ratio in this work is smaller than that of La substituted BFO-$PbTiO_3$. The reorientation of ferroelastic domains during mechanical loading occurs because it is energetically favorable.[35] It may be expected that if the lattice distortion is small, the energy gain achieved by the material from domain reorientation while under mechanical load is correspondingly small. This further implies that the critical stress required to achieve domain reorientation will be higher in materials with a low c/a-ratio such as 0.8BFT3 (c/a = 1.001).

The remanent strain of the materials increases with increasing temperature up to 200 °C (Figure 11a), opposite to what is observed for both hard and soft PZT.[46] The lattice distortion of 0.8BFT0 has been found to be relatively constant up to ~400 °C[15], while the coercive stress decreases with increasing temperature (Figure 11b). An increasing temperature will hence make domain switching easier (coercive stress decreases), while the potential strain from each reoriented polarization vector will remain constant. The theoretical maximum switching strain for single crystal 0.8BFT0, 0.8BFT1 and 0.8BFT3 is 0.77, 0.19 and 0.07 %, respectively, based on the room temperature lattice parameters.[52, 53] Only 28.5 % of these maximum values are theoretically achievable for randomly oriented polycrystals, resulting in a real maximum switching strain of 0.22, 0.05 and 0.02 % for the three materials, respectively.[52] The fact that the measured macroscopic strain is higher than the strain predicted by theory is probably related to challenges in resolving the lattice parameters from the obtained diffraction data. The domain size in ferroelastic materials may be influenced by the grain size.[54] It is, however, not likely that the variation of ferroelastic behavior observed for the different materials stems from a grain size effect, as the grain size was relatively constant for the materials subject to ferroelastic characterization.

The high ferroelectric-to-paraelectric phase transition temperature of the 0.8BFTy and 0.9BFTy series increases only slightly with increasing Ti substitution (Table 2). This is important knowledge as it rules out sub-T_C quenching as an explanation of the observed ferroelastic hardening. It also confirms that Ti-substitution can reduce the electrical conductivity of BFO-BKT without interfering with the high temperature applicability the material.

The effect of Ti substitution is different with respect to conductivity, lattice distortion and coercive stress in 0.8BFTy relative to 0.9BFTy. The effect of 1 mol% Ti substitution in 0.8BFTy/0.9BFTy is a reduced conductivity by four/two orders of magnitude (Figure 6), reduced lattice distortion by 75 %/9 % (Figure 3b) and an increased coercive stress by 48 %/>90 % (Figure 11b). Further work is required to determine whether these properties are correlated or why such differences are observed. The work presented herein and elsewhere[15] nevertheless provides important knowledge

for the understanding of the point defect chemistry of BFO that is essential for the future application of BFO ceramics as lead-free ferroelectrics.

2. Conclusions

The electrical conductivity of 0.8BFTy and 0.9BFTy was characterized with respect to Ti donor substitution, temperature and atmosphere. The conductivity was reduced by several orders of magnitude while retaining a high T_C. It was argued that the surplus charge of Ti^{4+} on a Fe^{3+} site is compensated by reducing the concentration of oxygen vacancies and reduction of the valence of Fe, giving a transition from p-type to n-type conductivity. The ferroelastic properties of 0.8BFTy and 0.9BFTy were shown to be highly dependent on thermal history, where a significant effect of thermal quenching was observed on both the coercive stress and remanent strain. The coercive stress decreases while the remanent strain increases with increasing temperature. The coercive stress is, however, relatively high at 400 °C compared to other investigated perovskite ferroelectrics. Finally, ferroelastic hardening was observed with increasing Ti substitution, suggesting that the concentration of oxygen vacancies is not the sole cause of hardening in BFO materials.

Acknowledgements

E.T.W, T.G and M.A.E gratefully acknowledge the support of the Research Council of Norway (FRINATEK project nr. 197497/F20). F.H.S. and K.G.W. gratefully acknowledge the support for their contributions from the Deutsche Forschungsgemeinschaft under WE4972/1-1 and WE4972/2-1.

References

1. J Rödel, W. Jo, K.T.P. Seifert, E.M. Anton, T. Granzow, D. Damjanovic, Perspective on the development of lead-free piezoceramics, J. Am. Ceram. Soc. 92 (2009) 1153-1177.
2. T. Rojac, A. Bencan, B. Malic, G. Tutuncu, J.L. Jones, J.E. Daniels, D. Damjanovic, $BiFeO_3$ Ceramics: Processing, electrical, and electromechanical properties, J. Am. Ceram. Soc. 97 (2014) 1993-2011.
3. G. Catalan, J.F. Scott, Physics and applications of bismuth ferrite, Adv. Mater. 21 (2009) 2463-2485.
4. M.M. Kumar, V.R. Palkar, K. Srinivas, S.V. Suryanarayana, Ferroelectricity in a pure $BiFeO_3$ Ceramic, Appl. Phys. Lett. 76 (2000) 2764-2766.
5. S.M. Selbach, T. Tybell, M.-A. Einarsrud, T. Grande, Structure and properties of multiferroic oxygen hyperstoichiometric $BiFe_{1\pm x}Mn_xO_{3+\delta}$, Chem. Mater. 21 (2009) 5176 -5186.
6. S.M. Selbach, T. Tybell, M.-A. Einarsrud, T. Grande, The ferroic phase transitions of $BiFeO_3$, Adv. Mater. 20 (2008) 3692.

7. T. Rojac, M. Kosec, B. Budic, N. Setter, D. Damjanovic, Strong ferroelectric domain-wall pinning in $BiFeO_3$ ceramics, J. Appl. Phys. 108 (2010) 074107.
8. M.I. Morozov, M.-A. Einarsrud, T. Grande, Atmosphere controlled conductivity and Maxwell-Wagner relaxation in $Bi_{0.5}K_{0.5}TiO_3$-$BiFeO_3$ ceramics, J. Appl. Phys. 115 (2014) 044104.
9. M.I. Morozov, M.-A. Einarsrud, T. Grande, Polarization and strain response in $Bi_{0.5}K_{0.5}TiO_3$-$BiFeO_3$ ceramics, Appl. Phys. Lett. 101 (2012) 252904.
10. J. Bennett, A.J. Bell, T.J. Stevenson, R.I. Smith, I. Sterianou, I.M. Reaney, T.P. Comyn, Multiferroic properties of $BiFeO_3$-$Bi_{0.5}K_{0.5}TiO_3$ ceramics, Mater. Lett. 94 (2013) 172-175.
11. H. Matsuo, Y. Noguchi, M. Miyayama, M. Suzuki, A. Watanabe, S. Sasabe, T. Ozaki, S. Mori, S. Torii, T Kamiyama, Structural and piezoelectric properties of high-density $(Bi_{0.5}K_{0.5})TiO_3$ $BiFeO_3$ ceramics, J. Appl. Phys. 108 (2010) 104103.
12. J.M. Kim, Y.S. Sung, J.H. Cho, T.K. Song, M.H. Kim, H.H. Chong, T.G. Park, D. Do, S.S. Kim, Piezoelectric and dielectric properties of lead-free $(1-x)(Bi_{0.5}K_{0.5})TiO_3$ -$xBiFeO_3$ ceramics, Ferroelectrics, 404 (2010) 88-92.
13. T. Ozaki, H. Matsuo, Y. Noguchi, M. Miyayama, S. Mori, Microstructures related to ferroelectric properties in $(Bi_{0.5}K_{0.5})TiO_3$-$BiFeO_3$, Jpn. J. Appl. Phys. 49 (2010) 09MC05.
14. M. Hagiwara, S. Fujihara, Effects of CuO addition on electrical properties of $0.6BiFeO_3$-$0.4(Bi_{0.5}K_{0.5})TiO_3$ lead-free piezoelectric ceramics J. Am. Ceram. Soc. 98 (2015) 469-475.
15. E.T. Wefring, M.-A. Einarsrud, T. Grande, Electrical conductivity and thermopower of $(1-x)BiFeO_3$ - $x\ Bi_{0.5}K_{0.5}TiO_3$ ($x = 0.1, 0.2$) ceramics near the ferroelectric to paraelectric phase transition, PCCP 17 (2015) 9420-9528.
16. C. F. Buhrer, Some properties of bismuth perovskites, J. Chem. Phys. 36 (1962) 798-803.
17. M.I. Morozov, M.-A. Einarsrud, T. Grande, Control of conductivity and electric field induced strain in bulk $Bi_{0.5}K_{0.5}TiO_3$-$BiFeO_3$ ceramics, Appl. Phys. Lett. 104 (2014) 122905.
18. Y.K. Jun, W.T. Moon, C.M. Chang, H.S. Kim, H.S. Ryu, J.W. Kim, K.H. Kim, S.H. Hong, Effects of Nb-doping on electric and magnetic properties in multiferroic $BiFeO_3$ ceramics , Solid State Commun. 135 (2005) 133-137.
19. X.D. Qi, J. Dho, R. Tomov, M.G. Blamire, J.L. MacManus-Driscoll, Greatly reduced leakage current and conduction mechanism in aliovalent-ion-doped $BiFeO_3$, Appl. Phys. Lett. 86 (2005) 062903.
20. K. Kalantari, I. Sterianou, S. Karimi, M.C. Ferrarelli, S. Miao, D.C. Sinclair, I.M. Reaney, Ti-Doping to reduce conductivity in $Bi_{0.85}Nd_{0.15}FeO_3$ ceramics Adv. Funct. Mater. 21 (2011) 3737-3743.
21. K. Abe, N. Sakai, J. Takahashi, H. Itoh, N. Adachi, T. Ota, Leakage current properties of cation-substituted $BiFeO_3$ ceramics, Jpn. J. Appl. Phys. 49 (2010) 09MB01.
22. G.D. Hu, S.H. Fan, C.H. Yang, W.B. Wu, Low leakage current and enhanced ferroelectric properties of Ti and Zn codoped $BiFeO_3$ thin film Appl. Phys. Lett. 92 (2008) 192905.
23. J. Mizusaki, T. Sasamoto, W.R Cannon, H.K. Bowen, Electronic conductivity, Seebeck coefficient, and defect structure of $La_{1-x}Sr_xFeO_3$ ($x=0.1, 0.25$), J. Am. Ceram. Soc. 66 (1983) 247-252.
24. O.F. Lohne, T.N. Phung, T. Grande, H.J.M. Bouwmeester, P.V. Hendriksen, M. Sogaard, K. Wiik, Oxygen non-stoichiometry and electrical conductivity of $La_{0.2}Sr_{0.8}Fe_{0.8}B_{0.2}O_{3-\delta}$, B= Fe, Ti, Ta, J. Electrochem. Soc. 161 (2014) F176-184.
25. G.L. Yuan, Y. Yang, S.W. Or, Aging-induced double ferroelectric hysteresis loops in $BiFeO_3$ multiferroic ceramic, Appl. Phys. Lett. 91 (2007) 122907.
26. S. Zhang, L. Wang, Y. Chen, D. Wang, Y. Yao, Y. Ma, Observation of room temperature saturated ferroelectric polarization in Dy substituted $BiFeO_3$ ceramics J. Appl. Phys. 111 (2012) 074105.
27. A. Y. Kim, Y. Lee, J. Kim, S. Han, H.-W. Kang, H.-G. Lee, C.J. Cheon, Effect of process condition on the ferroelectric properties in $BiFeO_3$-$(Bi,K)TiO_3$ ceramics, Korean Phys. Soc. 60 (2012) 83-86.

28. X. B. Ren, Large electric-field-induced strain in ferroelectric crystals by point defect-mediated reversible domain switching, Nat. Mater. 3 (2004) 91-94.
29. M.I. Morozov, D. Damjanovic, Charge migration in $Pb(Zr,Ti)O_3$ ceramics and its relation to ageing, hardening, and softening J. Appl. Phys. 107 (2010) 034106.
30. B. Jaffe, W.r. Cook, H.L. Jaffe, Piezoelectric ceramics, Academic Press: London, New York,, 1971.
31. K. Carl, K.H. Härdtl, Electrical after-effects in $Pb(Ti,Zr)O_3$ ceramics Ferroelectrics , 17 (1977) 473-486.
32. M. Morozov, Softening and hardening transitions in ferroelectric $Pb(Zr,Ti)O_3$ ceramics. EPFL, 2005.
33. M. S. Bernardo, T. Jardiel, M. Peiteado, F.J. Mompean, M. Garcia-Hernandez, M. A. Garcia, M. Villegas, A.C. Caballero, Intrinsic compositional inhomogeneities in bulk Ti-doped $BiFeO_3$: Microstructure development and multiferroic properties, Chem. Mater. 25 (2013) 1533-1541.
34. S.J. Kim, S.H. Han, H.G. Kim, A.Y. Kim, J.S. Kim, C.I. Cheon, Multiferroic properties of Ti-doped $BiFeO_3$ ceramics, J. Korean. Phys. Soc. 56 (2010) 439-442.
35. E. K. H. Salje, Phase transitions in ferroelastic and co-elastic crystals : an introduction for mineralogists, material scientists, and physicists - student edition. Cambridge University Press: Cambridge England ; New York, 1993.
36. E.T. Wefring, M.I. Morozov, M.-A. Einarsrud, T. Grande, Solid-state synthesis and properties of relaxor (1-x)BKT-xBNZ ceramics, J. Am. Ceram. Soc. 97 (2014) 2928-2935.
37. Coelho, A. A. TOPAS Academic: General Profile and Structure Analysis Software for Powder Diffraction Data; Bruker AXS: Karlsruhe, Germany, 2004.
38. K. G. Webber, E. Aulbach, T. Key, M. Marsilius, T. Granzow, J. Rödel, J. Acta Mater. 57 (2009) 4614.
39. T. Leist, K.G. Webber, W. Jo, T. Granzow, E. Aulbach, J. Suffner, J. Rödel, Mechanical versus electrical loading in La-doped bismuth ferrite-lead titanate, J. Appl. Phys. 109 (2011) 054109.
40. Y. H. Seo, M. Vogler, D. Isaia, E. Aulbach, J. Rödel, K.G. Webber, Temperature-dependent R-curve behavior of $Pb(Zr_{1-x}Ti_{-x})O_3$, Acta Mater. 61 (2013) 6418.
41. S. M. Selbach, T. Tybell, M.-A. Einarsrud, T. Grande, Phase transitions, electrical conductivity and chemical stability of $BiFeO_3$ at high temperatures, J. Solid State Chem. 183 (2010) 1205-1208.
42. Y. Wang, C.-W. Nan, Enhanced ferroelectricity in Ti-doped multiferroic $BiFeO_3$ thin films , Appl. Phys. Lett. 89 (2006) 052903.
43. N. Maso, A.R. West, Electrical properties of Ca-doped $BiFeO_3$ ceramics: From p-type semiconduction to oxide-ion conduction , Chem. Mater. 24 (2012) 2127-2132.
44. W.T. Chen, A.J. Williams, L. Ortega-San-Martin, M. Li, D.C. Sinclair, W.Z. Zhou, J.P. Attfield, Robust antiferromagnetism and structural disorder in $Bi_xCa_{1-x}FeO_3$ perovskites Chem. Mater. 21 (2009) 2085-2093.
45. F.H. Schader, M.I. Morozov, E.T. Wefring, T. Grande, K.G. Webber, Mechanical stability of polar defects in ferroelectric perovskites J. Appl. Phys. 117 (2015) 194101.
46. M. Marsilius, K.G. Webber, E. Aulbach, T. Granzow, Comparison of the temperature-dependent ferroelastic behavior of hard and soft lead zirconate titanate ceramics, J. Am. Ceram. Soc. 93 (2010) 2850-2856.
47. J. Seidel, L.W. Martin, Q. He, Q. Zhan, Y.H. Chu, A. Rother, M.E. Hawkridge, P. Maksymovych, P. Yu, M. Gajek, N. Balke, S.V. Kalinin, S. Gemming, F. Wang, G. Catalan, J.F. Scott, N. Spaldin, J. Orenstein, R. Ramesh, Conduction at domain walls in oxide multiferroics, Nat. Mater. 8 (2009) 229-234.
48. J. Seidel, P. Maksymovych, Y. Batra, A. Katan, S.Y. Yang, Q. He, A.P. Baddorf, S. V. Kalinin, C.H. Yang, J.C. Yang, Y.H. Chu, E.K.H. Salje, H. Wormeester, M. Salmeron, R. Ramesh, Domain wall conductivity in La-doped $BiFeO_3$, Phys. Rev. Lett. 105 (2010) 197603.

49. S. Farokhipoor, B. Noheda, Conduction through 71˚ domain walls in $BiFeO_3$ thin films, Phys. Rev. Lett. 107 (2011) 127601.
50. P. Maksymovych, J. Seidel, Y.H. Chu, P.P. Wu, A.P. Baddorf, L.Q. Chen, S.V. Kalinin, R. Ramesh, Dynamic conductivity of ferroelectric domain walls in $BiFeO_3$, Nano Lett. 11 (2011) 1906-1912.
51. X.H. Zheng, Z.H. Ma, P.J. Chen, D.P. Tang, N. Ma, Decomposition behavior and dielectric properties of Ti-doped $BiFeO_3$ ceramics derived from molten salt method, J. Mater. Sci.-Mater. El. 23 (2012) 1533-1537.
52. J.L. Jones, M. Hoffman, K.J. Bowman, Saturated domain switching textures and strains in ferroelastic ceramics, J. Appl. Phys. 98 (2005) 024115.
53. H.D. Megaw, C.N.W. Darlington, Acta Cryst. A A31 (1975) 161.
54. W.W. Cao, C.A. Randall, Grain size and domain size relations in bulk ceramic ferroelectric materials, J. Phys. Chem. Solids 57 (1996) 1499-1505.